Philosophical Magazine A

ISSN: 0141-8610 (Print) 1460-6992 (Online) Journal homepage: http://www.tandfonline.com/loi/tpha20

Texturing of the upper mantle during convection

Paul R. Dawson & H.-R. Wenk

To cite this article: Paul R. Dawson & H.-R. Wenk (2000) Texturing of the upper mantle during convection, Philosophical Magazine A, 80:3, 573-598, DOI: 10.1080/01418610008212069

To link to this article: http://dx.doi.org/10.1080/01418610008212069

PHILOSOPHICAL MAGAZINE A, 2000, VOL. 80, NO. 3, 573–598

Texturing of the upper mantle during convection

PAUL R. DAWSON†

Sibley School of Mechanical and Aerospace Engineering, Cornell University, Ithaca, New York, USA

and H.-R. WENK

Department of Geology and Geophysics, University of California, Berkeley, California, USA

[*Received 6 March 1998 and accepted 28 April 1999*]

ABSTRACT

Convection of rocks in the Earth's mantle gives rise to crystallographic texture of the constituent mineral, olivine. In this paper, we present simulations of texturing of olivine as it flows through a two-dimensional, buoyancy-driven convection cell. The simulations utilize a finite-element formulation for coupled heat transfer and viscoplastic flow, together with polycrystal plasticity, to evaluate the deformation of rocks within the convection cell and the consequent texture evolution in the upper mantle. From the computed texture field, which varies considerably over the cell, the seismic velocity distribution is evaluated. Seismic velocity variations are presented and discussed in the context of earthquake travel time observations and tomographic maps.

§1. INTRODUCTION

Of particular importance for processes in the crust, such as volcanic activity, earthquakes and mountain building, is the deformation of the mantle. Geophysicists have firmly established that, within the mantle, large cells of convection are induced by instabilities and driven by temperature and density gradients. This convective flow has been modelled by geophysicists since the early 1960s beginning with single two-dimensional cells and progressing to three-dimensional geometries involving many interacting cells (for example Turcotte and Oxburgh (1967), McKenzie (1979), Hager and O'Connell (1981), King *et al.* (1990), Glatzmaier and Schubert (1993), Tackley *et al.* (1993), Bunge and Baumgardner (1995), and Bunge *et al.* (1996)). In general, the models proposed in these investigations are based on the assumption that the material is a viscous liquid in the sense that the shear stress is proportional to the shear strain rate. Neither the internal structure nor the directionality of the properties is considered in assessing the properties of the mantle rocks. Yet a specific and unique property of the solid state is its regular internal structure and anisotropy. The convective flow of the mantle substantially alters the internal structure, and the mechanical properties derived from it.

The main constituent of the upper mantle is olivine, which exhibits about a 25% difference in acoustic speed between the slowest and the fastest crystal directions.

† Author for correspondence.

Philosophical Magazine A ISSN 0141–8610 print/ISSN 1460-6992 online © 2000 Taylor & Francis Ltd
http://www.tandf.co.uk/journals/tf/01418610.html

Because of this difference, a polycrystal with preferred orientations of component crystals will display a directional dependence (anisotropy) of seismic wave propagation. Indeed, seismic waves do travel faster (about 5%) perpendicular to the oceanic ridges than parallel to them (Morris *et al.* 1969). About 35 years ago, Hess (1964) interpreted this as a result of a preferential alignment of crystals with directional properties and proposed that this alignment was attained during mantle convection. While the general concept of preferred orientation (referred to as crystallographic texture, or simply texture hereafter) has been widely accepted, most simulations of the mantle convection are still performed using isotropic continuum theories, mainly because of the great complexities that crystallographic models entail.

In a prior publication, a model was presented for predicting the development of anisotropy in a convection cell and discussed implications for convection in the Earth's mantle (Chastel *et al.* 1993). The results indicate that during convection, crystals reorient into characteristic textures that cause anisotropic physical properties. It was observed that these patterns are highly heterogeneous over the span of the convection cell and depend on the specific straining history along individual streamlines of the cell. The rotations that reorient crystal lattices are due to the activation of slip systems in deforming single crystals as well as the macroscopic rotation of material progressing along a streamline. Both of these are most intense during upwelling at ridges and during subduction. Thus, texture development is particularly strong in these regions. Using the crystallographic texture throughout the convection cell and the physical properties of single crystals, seismic velocity averages over mantle sectors were computed and the directional dependence of wave propagation determined. The predicted azimuthal variation in p-wave anisotropy of 5–10% reported in that publication agrees well with actual observed values.

The evolution of crystallographic texture also has been studied for a more local mantle deformation, along a spreading ridge, to distinguish between the anisotropies produced by passive and buoyant flows (Blackman *et al.* 1996). The passive velocity field was computed by requiring that the surface velocity equalled the spreading rate; the buoyant velocity field resulted from the variations in body forces that arise from differing amounts of thermal expansion in the presence of temperature gradients. Very different texture fields develop for the two cases, together with the associated differences in computed seismic travel times across ridges. These results were used to estimate whether the observed travel times could be used to distinguish between the two cases.

The convection cell used in the earlier study was highly arbitrary and idealized. In the investigation reported here we are using a more realistic mantle, one with dimensions corresponding to those in the Earth and with material properties that are closer to those which are believed to exist. We discretize the convective cell with a greater number of finite elements to resolve the gradients of the flow better and use a larger number of crystals to represent each polycrystal. Apart from that, the procedure is similar. The 'mantle' which we simulate is still idealized; the model is two dimensional, there is no interaction with the crust (e.g. during subduction) and the sole phase change (at 650 km) affects only the mechanical properties. The model is intentionally kept simple to emphasize the effects of the convective flow on the internal structure of the mantle material and on the resulting anisotropy in its mechanical properties. We begin with a brief review of the significant elements of the model and simulation procedures and refer the reader for details to the previous study.

§2. Approach

The Earth is a very heterogeneous system at all scales. There are compositional and structural variations both laterally and with depth. Deformation occurs at the large macroscopic level down to the atomic structure within crystals. Because of this complexity there is limited utility in modelling deformation using an approach that is restricted to the macroscopic scale wherein the mantle is treated as a continuum. Instead, we use an approach that combines models from two scales. At the macroscopic level the finite-element method is ideally suited to deal with the heterogeneous deformation patterns present over the dimensions of a convective cell, and to resolve gradients in the flow field associated with deformation and rotation of the mantle minerals. At the microscopic level, polycrystal plasticity theory simulates deformation processes within crystals, deformations that drive the microstructural change of the mantle minerals and that are inherited from the macroscopic flow within the cell.

The finite-element method provides a means to solve a system of model equations that incorporate the physical realities of a heterogeneous macroscopic system. The methodology for obtaining a solution is an integral part of a complete simulation model. Central to the model are the governing equations, which include the balance laws for momentum, mass and energy, the boundary conditions and the equations of polycrystal plasticity. The finite-element method is chosen for its ability to deliver accurate numerical solutions for this system of nonlinear inhomogeneous time-dependent partial differential equations. The finite-element method is widely used in geodynamics. What is new is that we introduce anisotropy through a physically meaningful polycrystal plasticity model. This approach has first been developed for metal-forming applications (Mathur *et al.* 1990, Beaudoin *et al.* 1993, 1994) that share many of the same features, such as large strain deformations, coupled heat transfer and plastic flow, and evolving material microstructure. Properties within a finite element are defined from the average responses of a population of crystals that serves as a sample of the material existing within the element. The crystals dimensions are typically much smaller than that of the element, so that the crystal aggregate (referring to the sample of crystals drawn from the population) numbers far fewer than the number of crystals that would actually exist in a volume comparable with that of the element.

Simulations that employ finite elements whose dimensions are far larger than that of an aggregate of crystals within it entails some assumptions with respect to linking the *macroscopic* element and *microscopic* crystal scales. In the case of metals the results of simulations can be directly compared with experiments. In the case of the Earth's interior, deformation processes have been subject to a long history which are only in a very limited way accessible to experimentation. Furthermore, many properties of the material which composes the interior of the Earth are only inferred from indirect observations. Nevertheless, many mechanisms are presumably similar to those in metal forming and, with some modifications, a similar approach is applicable.

§3. Single-crystal constitutive behaviour

3.1. *Slip systems*

The mechanisms that contribute to the plastic deformations of minerals are dependent on the strain rate and the temperature (Nicolas *et al.* 1971, Kohlstedt and Goetze 1974, Bai *et al.* 1991, Karato *et al.* 1995). Depending on the regime of

strain rate and temperature, some mechanisms will dominate over others and be principally responsible for shape changes occurring in the material. Here, we assume that the crystals are deforming solely by slip, rather than by other mechanisms or by combinations of mechanisms. Although slip occurs by the motion of dislocations through the lattice, we do not resolve the behaviour of individual dislocations. Rather, the net effect of dislocation motion is captured by the activity of slip systems, each of which contributes to a single shear mode of deformation.

A slip system can be described mathematically by vectors that describe the normal to the slip plane ($\mathbf{m}$) and the slip direction ($\mathbf{s}$) (Kocks *et al.* 1998). Forming the tensor product of these gives the Schmid tensor

$$\mathbf{T} = \mathbf{s} \otimes \mathbf{m}, \tag{1}$$

which has symmetric and skew parts denoted by

$$\mathbf{P} = \mathrm{sym}\,(\mathbf{T}) \tag{2}$$

and

$$\mathbf{Q} = \mathrm{skew}\,(\mathbf{T}). \tag{3}$$

Minerals often exhibit only a few potentially active slip systems. However, it takes five independent slip systems to accommodate all five deviatoric components in $\mathbf{D}'$. For olivine the predominant slip systems are (Kohlstedt and Goetze 1974, Durham and Goetze 1977)

$$\mathbf{m} = (010), \quad \mathbf{s} = [100],$$
$$\mathbf{m} = (001), \quad \mathbf{s} = [100],$$
$$\mathbf{m} = (010), \quad \mathbf{s} = [001],$$
$$\mathbf{m} = (100), \quad \mathbf{s} = [001],$$

which define only four slip systems which are all orthogonal.

With the slip systems defined, the plastic velocity gradient $\mathbf{L}^{\mathrm{p}}$ in a crystal is written as a combination of the slip system responses:

$$\mathbf{L}^{\mathrm{p}} = \sum_{\alpha} \mathbf{T}^{\alpha} \dot{\gamma}^{\alpha}, \tag{4}$$

where $\dot{\gamma}^{\alpha}$ is the rate of shear on the α slip system. (A superscript α is used to designate one of the systems.) This relationship is a central part of the mathematical structure of polycrystal plasticity as it relates the net result of dislocation movement to crystal shape change and lattice rotation.

3.2. *Crystal kinematics*

A comprehensive treatment of the crystal kinematics begins with the mapping of coordinates of points within the crystal over time (Dawson and Marin 1997). This mapping is the motion of the crystal and is given by

$$\mathbf{x} = \mathbf{x}(\mathbf{X}, t), \tag{5}$$

in which $\mathbf{x}$ are the current coordinates and $\mathbf{X}$ are reference coordinates. From the mapping the crystal deformation gradient $\mathbf{F}^{\mathrm{c}}$, is determined as

$$\mathbf{F}^{\mathrm{c}} = \frac{\partial \mathbf{x}}{\partial \mathbf{X}} \tag{6}$$

in the usual way. The full deformation gradient is decomposed into several parts

$$\mathbf{F}^{c} = \mathbf{V}^{*}\mathbf{R}^{*}\mathbf{F}^{p}, \tag{7}$$

where $\mathbf{V}^{*}$ is the elastic stretch, $\mathbf{R}^{*}$ is the lattice rotation and $\mathbf{F}^{p}$ is the plastic deformation gradient. We restrict our attention now to the inelastic response, assuming that the elastic strains are always small in relation to unity, such that $\mathbf{V}^{*} \approx \mathbf{I}$. The crystal deformation gradient then becomes

$$\mathbf{F}^{c} = \mathbf{R}^{*}\mathbf{F}^{p}, \tag{8}$$

which is differentiated with respect to time and divided into symmetric and skew parts to give

$$\mathbf{D}^{c} = \mathbf{D}^{p} = \sum_{\alpha} \dot{\gamma}^{\alpha}\mathbf{P}^{\alpha} \tag{9}$$

and

$$\mathbf{W}^{c} = \dot{\mathbf{R}}^{*}\mathbf{R}^{*T} + \sum_{\alpha} \dot{\gamma}^{\alpha}\mathbf{Q}^{\alpha} = \dot{\mathbf{R}}^{*}\mathbf{R}^{*T} + \mathbf{W}^{p}. \tag{10}$$

where $\mathbf{D}^{c}$ is the crystal deformation rate, $\mathbf{D}^{p}$ is the plastic deformation rate, $\mathbf{W}^{c}$ is the crystal spin and $\mathbf{W}^{p}$ is the plastic spin. Equation (9) relates the crystal shape change to the net motion of dislocations, while equation (10) provides a relation between the crystal spin and the lattice orientation. Together, $\mathbf{D}^{p}$ and $\mathbf{W}^{p}$ form the plastic velocity gradient given in equation 4.

3.3. *Crystal compliance and stiffness*

The above kinematic framework is not sufficient by itself to define the crystal stiffness; a relationship between the crystal deviatoric stress $\boldsymbol{\sigma}^{c}$ and slip system shearing rates $\dot{\gamma}$ is also required. (Primed quantities are deviatoric throughout the paper.) This is obtained from the kinetic relation for slip on a slip system and the geometric relation between the crystal stress and its component on the slip plane and in the slip direction. The kinetics of slip is assumed to be well represented with a power-law relation (Durham and Goetze 1977), as discussed in more detail for olivine later. For the time being we assume that such a relation is valid, and proceed to establish the stiffness using

$$\dot{\gamma}^{\alpha} = \dot{\gamma}_{0}\left|\frac{\tau^{\alpha}}{\tau_{c}}\right|^{1/m} \operatorname{sgn}(\tau^{\alpha}) = f(\tau^{\alpha}, \tau_{c}), \tag{11}$$

where m is the strain rate sensitivity, $\dot{\gamma}_{0}$ is a model parameter, τ_{c} is the temperature-dependent slip system strength and τ^{α} is the resolved shear stress for the αth system. The resolved shear stress is

$$\tau^{\alpha} = \mathbf{P}^{\alpha} \cdot \boldsymbol{\sigma}'^{c}. \tag{12}$$

Factoring a term that is linear in τ^{α} from equation (11) and combining this with equations (9) and (12) give (Dawson and Marin 1997)

$$\mathbf{D}'^{c} = \mathcal{M}^{c} \cdot \boldsymbol{\sigma}'^{c}, \tag{13}$$

where

$$\mathcal{M}^{c} = \sum_{\alpha} \frac{f(\tau^{\alpha}, \tau_{c})}{\tau^{\alpha}} \mathbf{P}^{\alpha}\mathbf{P}^{\alpha T}. \tag{14}$$

Inverting equation (13) gives

$$\boldsymbol{\sigma}'^{c} = \boldsymbol{\mathcal{M}}^{c^{-1}} \cdot \mathbf{D}'^{c} = \boldsymbol{\mathcal{S}}^{c} \cdot \mathbf{D}'^{c}. \tag{15}$$

The compliance $\boldsymbol{\mathcal{M}}^{c}$ or the stiffness $\boldsymbol{\mathcal{S}}^{c}$ is used in constructing the macroscopic stiffness $\boldsymbol{\mathcal{S}}$ in accordance with the assumptions that link the crystal and macroscopic scales, discussed in the following section.

3.4. *Olivine parameters*

As was mentioned above, we assume that the upper mantle is composed of the mineral olivine and the lower mantle of a mineral phase that is ten times more viscous than olivine, in accordance with implied mechanical properties for magnesiowuestite and Mg–Si perovskite. Furthermore, since it was assumed that no anisotropy exists in the lower mantle, it was unnecessary to know slip systems for the lower mantle phase and an isotropic viscosity that only changes with temperature was used. The mechanical properties of olivine, particularly slip systems, critical shear stresses and their temperature dependence, and the strain-rate sensitivity were derived from reported experiments (Kohlstedt and Goetze 1974, Durham and Goetze 1977 and Bai *et al.* 1991) and are summarized in table 1. From experimental data (Bai *et al.* 1991), critical shear stresses were assigned on the basis of a strain rate of $10^{-5}\,s^{-1}$, an orthopyroxene buffer and an oxygen fugacity $f_O = 10^{4.5}$ atm for high-temperature conditions. The experimental data are limited and values for reference conditions had to be extrapolated. For the temperature sensitivity of the critical stress we used an exponential law

$$\tau_c = \tau_0 \exp\left[b\left(\frac{1}{T} - \frac{1}{T_{ref}}\right)\right], \tag{16}$$

where τ_c is the slip system strength at temperature T, and τ_0 the slip system strength at a reference temperature T_{ref}. It was assumed that T_{ref} and b are the same for all slip systems. As reference temperature we chose 1673 K. The τ_0 values are different for the different slip systems and values were estimated from mechanical data for compression experiments in different sample orientations. The factor b was evaluated from data for 1533 and 1623 K for (010)[100] slip and a value of $15.5 \times 10^3\,K^{-1}$ was obtained. For the description of the dependence of the stress on the strain rate, the power-law relation in equation (11) was prescribed using a stress exponent $1/m$ of 3.7 all slip systems (Durham and Goetze 1977). With these values, stress–strain curves for simple deformation histories were calculated directly with the polycrystal plasticity model, as shown in figure 1 for axisymmetric compression at several temperatures. The effective stress smoothly increases to an effective strain of 0.3

Table 1. Slip systems and derived slip system strengths for olivine at 1673 K (Bai *et al.* 1991).

Slip system	Experimental crystal orientation	Reference strength (MPa)
(010)[100]	$[110]_c$	18
(001)[100]	$[101]_c$	18
(100)[001]	$[101]_c$	18
(010)[001]	$[011]_c$	45

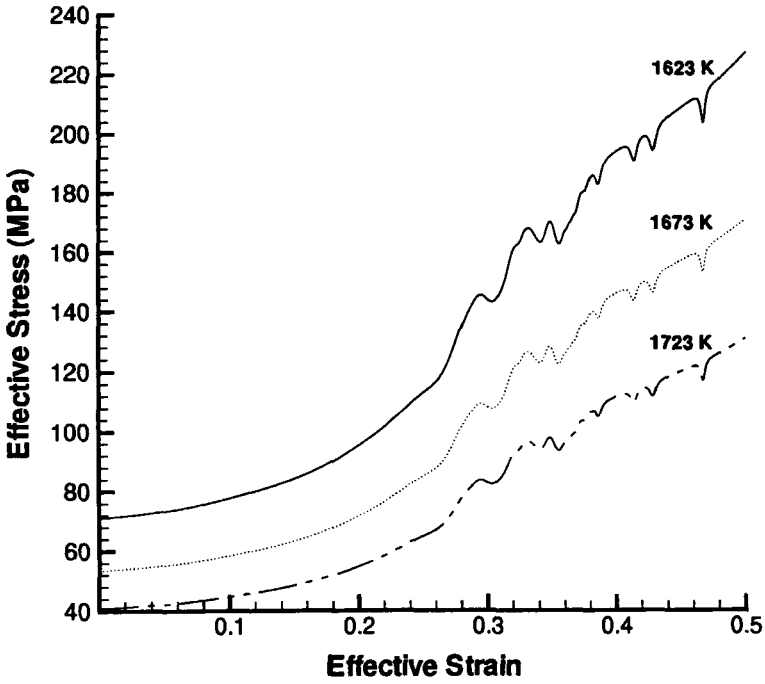

Figure 1. Calculated olivine stress–strain curves for axisymmetric compression at several temperatures.

for all temperatures. Above a strain of 0.3 the effective stress continues to rise but exhibits oscillations of several per cent of the maximum value. These oscillations are not uncommon in the stress computed using an equilibrium-based model, as is used in this paper, owing to the sensitivity of the stress to evolving texture. Although a small amount of slip system hardening often will eliminate the oscillations, this was not critical to the simulations presented here, and a constant value of strength was used for each slip system throughout.

§4. Polycrystal constitutive equations

4.1. *Orientational averages*

In the class of applications that we consider here, every macroscopic point has associated with it a representation of the crystallographic texture of a small volume of material containing the point. We refer to the orientations that comprise the volume as an aggregate, whether we represent the orientations with a discrete set of orientations or by a probability density function A that prescribes an orientation distribution (Kumar and Dawson 1996). Although these two approaches appear to be quite different idealizations of the texture, they fall within the same general framework, as presented in this section. The texture enters the simulations through the determination of mechanical properties at the macroscopic level. The macroscopic stiffness is obtained by averaging the crystal stiffness (or by inverting the average of the crystal compliance) for all crystals within the aggregate. This requires that the crystallographic texture be available at each instant when the velocity field is computed. For this purpose, we present methods for evolving the texture for

imposed deformation histories, histories that will be evaluated as part of the full simulation procedure.

The orientation distribution associated with an aggregate is given by the probability density $A(\mathbf{r})$ with the property that the volume fraction of crystals v_f^* in a subset of orientation space Ω^* is given by

$$v_f^* = \int_{\Omega^*} A(\mathbf{r})\, d\Omega. \tag{17}$$

where Ω is the domain of orientation space and $\mathbf{r}$ is the vector describing the crystal orientation using an angle-axis representation (Kumar and Dawson 1998). $A(\mathbf{r})$ is normalized such that

$$\int_{\Omega} A(\mathbf{r})\, d\Omega = 1. \tag{18}$$

The extent of the domain Ω depends on the specific parametrization of orientation space and the symmetries exhibited by the crystal (Kumar and Dawson 1998).

The macroscopic behaviour is the average of the behaviours of the individual crystals of the aggregate. We obtain the average by an integration of the crystal quantity, weighted by the probability density, over orientation space. For an arbitrary crystal quantity Γ^c the average value $\langle \Gamma^c \rangle$, is given by (Kumar and Dawson 1996)

$$\Gamma = \langle \Gamma^c \rangle = \int_{\Omega} \Gamma^c(\mathbf{r}) A(\mathbf{r})\, d\Omega. \tag{19}$$

In particular, we require that the deviatoric stress and deformation rate at the macroscopic level reflect the average of their counterparts at the crystal level so that

$$\mathbf{D}' = \langle \mathbf{D}'^c \rangle = \int_{\Omega} \mathbf{D}'^c(\mathbf{r}) A(\mathbf{r})\, d\Omega \tag{20}$$

and

$$\boldsymbol{\sigma}' = \langle \boldsymbol{\sigma}'^c \rangle = \int_{\Omega} \boldsymbol{\sigma}'^c(\mathbf{r}) A(\mathbf{r})\, d\Omega. \tag{21}$$

In instances in which the aggregate consists of a discrete sample of orientations taken from the orientation distribution, the macroscopic values are simply the weighted averages of the crystal quantities

$$\mathbf{D}' = \langle \mathbf{D}'^c \rangle = \sum_c w^c \mathbf{D}'^c \tag{22}$$

and

$$\boldsymbol{\sigma}' = \langle \boldsymbol{\sigma}'^c \rangle = \sum_c w^c \boldsymbol{\sigma}'^c, \tag{23}$$

where w^c is a set of weights assigned with one-to-one correspondence to the orientations (Beaudoin *et al.* 1993). The values of elements of this set are chosen to emphasize those crystals corresponding to regions in the orientation domain where A is high.

4.2. *Linking crystal responses to continuum scale motion*

Recall from equations (14) and (15) that the relationship between the deformation rate and deviatoric stress in a single crystal is an invertible relationship of the form

$$\mathbf{D}'^{c} = \mathcal{M}^{c} \cdot \boldsymbol{\sigma}'^{c} \tag{24}$$

or

$$\boldsymbol{\sigma}'^{c} = \mathcal{S}^{c} \cdot \mathbf{D}'^{c} = (\mathcal{M}^{c})^{-1} \cdot \mathbf{D}'^{c}, \tag{25}$$

where $\mathcal{M}^{c}$ and $\mathcal{S}^{c}$ are the single-crystal viscoplastic compliance and stiffness respectively. If we proceed with averaging these relationships we obtain

$$\langle \mathbf{D}'^{c} \rangle = \langle \mathcal{M}^{c} \cdot \boldsymbol{\sigma}'^{c} \rangle \tag{26}$$

and

$$\langle \boldsymbol{\sigma}'^{c} \rangle = \langle \mathcal{S}^{c} \cdot \mathbf{D}'^{c} \rangle. \tag{27}$$

On the macroscopic scale, we assume the deviatoric stress and deformation rate are related in an analogous form

$$\boldsymbol{\sigma}' = \mathcal{S} \cdot \mathbf{D}', \tag{28}$$

To relate equations (26) and (27) with equation (28), we must specify the nature of the link between the microscopic (single crystal) and macroscopic behaviour. This link is often referred to as the mean-field assumption or partitioning rule. It defines the manner in which some macroscopic quantity, such as the deformation rate, is distributed over the crystals of an aggregate. Two extreme possibilities are that the deformation rates are identical from crystal to crystal over an aggregate, as proposed by Taylor and Elam (1923) and Taylor (1938), and that the stresses are identical in each crystal (Prantil *et al.* 1995), which can be thought of as an extension to the hypothesis of Sachs (1928). For the first case we note that in equation (27), the crystal deformation rate can be removed from the orientation average if these rates are identical for all orientations to give

$$\boldsymbol{\sigma}' = \langle \boldsymbol{\sigma}'^{c} \rangle = \langle \mathcal{S}^{c} \cdot \mathbf{D}'^{c} \rangle = \langle \mathcal{S}^{c} \rangle \cdot \mathbf{D}' = \mathcal{S} \cdot \mathbf{D}'. \tag{29}$$

Using this assumption renders equal straining in all crystals of an aggregate. For the second case, the identical stress may be taken outside the orientational average to give

$$\mathbf{D}' = \langle \mathbf{D}'^{c} \rangle = \langle \mathcal{M}^{c} \cdot \boldsymbol{\sigma}'^{c} \rangle = \langle \mathcal{M}^{c} \rangle \cdot \boldsymbol{\sigma}'^{c} = \langle \mathcal{M}^{c} \rangle \cdot \boldsymbol{\sigma}'. \tag{30}$$

To obtain the form of equation (28), $\langle \mathcal{M}^{c} \rangle$ is inverted:

$$\boldsymbol{\sigma}'^{c} = \langle \mathcal{M}^{c} \rangle^{-1} \cdot \mathbf{D}'^{c}. \tag{31}$$

Estimating $\mathcal{S}$ by these two approaches gives upper and lower bounds respectively of the stiffness for a specific texture. With the Taylor hypothesis, compatibility is enforced, but equilibrium may be violated. With the equal-stress constraint, equilibrium is satisfied identically, but the crystal deformations may not be compatible. For olivine, the limited number of independent slip systems is inconsistent with use of the Taylor hypothesis; so we have employed the lower bound approach in the computations presented. It has been established previously (Wenk *et al.* 1991,

Chastel *et al.* 1993) that results of polycrystal plasticity simulations for simple strain histories agree closely with those observed in experiments (Nicolas *et al.* 1973).

§5. Finite-element procedure

The balance laws are used to form the residuals for the finite-element approximations constructed to evaluate the velocity and temperature fields. Here we discuss only the solution for the workpiece motion, as the temperature distribution is obtained with standard methodologies (Zienkiewicz and Taylor 1990). A weighted residual for equilibrium (Johnson 1987) is written over the body volume $\mathcal{B}$ using vector weights, as

$$R_u = \int_{\mathcal{B}} \boldsymbol{\psi} \cdot (\nabla \boldsymbol{\sigma}^{\mathrm{T}} + \mathbf{b}) \, \mathrm{d}\mathcal{B}. \tag{32}$$

This is modified to obtain the weak form through integration by parts and application of the divergence theorem to give

$$R_u = -\int_{\mathcal{B}} \mathrm{Tr}\,(\boldsymbol{\sigma}'^{\mathrm{T}} \cdot \mathrm{grad}\,\boldsymbol{\psi}) \, \mathrm{d}\mathcal{B} + \int_{\mathcal{B}} p \,\mathrm{div}\,\boldsymbol{\psi} \, \mathrm{d}\mathcal{B} + \int_{\partial\mathcal{B}} \mathbf{t} \cdot \boldsymbol{\psi} \, \mathrm{d}\Gamma + \int_{\mathcal{B}} \mathbf{b} \cdot \boldsymbol{\psi} \, \mathrm{d}\mathcal{B}, \tag{33}$$

where the Cauchy stress has been divided into its deviatoric and volumetric parts according to

$$\boldsymbol{\sigma} = \boldsymbol{\sigma}' + \sigma_{\mathrm{m}} \mathbf{I}, \tag{34}$$

with σ_{m} being the mean stress and $\mathbf{t}$ is the traction acting on the boundary $\partial\mathcal{B}$ of $\mathcal{B}$. For an incompressible medium

$$\mathrm{Tr}\,\mathbf{D} = \mathrm{div}\,\mathbf{u} = 0, \tag{35}$$

which can be enforced using a consistent penalty approach (Engleman *et al.* 1982). First a residual is written using the incompressibility constraint (equation (35))

$$R_{\mathrm{m}} = \int_{\mathcal{B}} \phi \,\mathrm{div}\,\mathbf{u} \, \mathrm{d}\mathcal{B}, \tag{36}$$

where ϕ are scalar weights. Slight compressibility is admitted, giving the possibility to write a penalty constraint in a form consistent with the finite element discretization

$$R_{\mathrm{m}} = \int_{\mathcal{B}} \phi \sigma_{\mathrm{m}} \, \mathrm{d}\mathcal{B} + \frac{1}{\epsilon} \int_{\mathcal{B}} \phi \,\mathrm{div}\,\mathbf{u} \, \mathrm{d}\mathcal{B}, \tag{37}$$

where ϵ is a penalty parameter. Finite-element interpolation is introduced as

$$\mathbf{u} = [N]\{U\}, \tag{38}$$

$$\sigma_{\mathrm{m}} = [N_{\mathrm{p}}]\{P\}, \tag{39}$$

for the trial functions and

$$\boldsymbol{\psi} = [N]\{\Psi\}, \tag{40}$$

$$\phi = [N_{\mathrm{p}}]\{\Phi\}, \tag{41}$$

for the weighting functions where N and N_{p} are functions of the position $\mathbf{x}$. The trial functions for $\mathbf{u}$ are continuous over element boundaries but, for σ_{m}, discontinuous interpolation is specified to match the interpolation for the gradient of the velocity.

With discontinuous pressure interpolation, the penalized incompressibility constraint can be written element by element as

$$\{P\} = -\frac{1}{\epsilon}[M_p]^{-1}[G]^T\{U\}, \tag{42}$$

where

$$[M_p] = \int_{\mathcal{B}} [N_p]^T[N_p]\, d\mathcal{B} \tag{43}$$

and

$$[G] = \int_{\mathcal{B}} [B]^T\{h\}[N_p]\, d\mathcal{B}. \tag{44}$$

$[B]$ contains spatial derivatives of $[N]$ such that

$$\{D\} = [B]\{U\}. \tag{45}$$

$\{D\}$ is a vector containing the components of the deformation rate and $\{h\}$ is the trace operator. We introduce the mechanical behaviour from equation (28) in matrix form as

$$\{\sigma'\} = [\mathcal{S}]\{D'\}. \tag{46}$$

Substitution of this relationship into equation (33) eliminates the deviatoric stress. Taken with equation (42) for eliminating the pressure, the residual is written for arbitrary variations in the weights as

$$([K_s] + [K_v])\{U\} = \{F\}, \tag{47}$$

where

$$[K_s] = \int_{\mathcal{B}} [B]^T[\mathcal{S}][B]\, d\mathcal{B} \tag{48}$$

$$[K_v] = -\frac{1}{\epsilon}[G][M_p]^{-1}[G]^T \tag{49}$$

and

$$\{F\} = \int_{\partial\mathcal{B}} [N]^T\{t\}\, d\Gamma + \int_{\mathcal{B}} [N]^T\{b\}\, d\mathcal{B}. \tag{50}$$

From equation (47), the velocity field is determined for a specific combination of geometry, loading and state. The driving force for the flow arises from the density gradients associated with the non-uniform temperature field. To accommodate this, an iterative procedure is used to couple the heat transfer solution with the solution for the velocity field.

The macroscopic material stiffness given by equation (28) is derived as the average of single-crystal responses using either an upper or a lower bound assumption. The slip system response for the single crystals is determined by matching laboratory data for the compression of an olivine sample, as discussed earlier. In the previous study (Chastel *et al.* 1993) the lower bound stiffness was used in the finite-element equations, and convective velocity fields were computed for two different sets boundary conditions. Each set restricted the magnitude of the velocity to be consistent with observed convection rates. Here, we replace the anisotropic stiffness derived in this

way with an isotropic stiffness based on a single viscosity and do not have to place an explicit constraint on the magnitude of the velocity field. The reason for making this change is that the viscosity derived from laboratory experiments is orders of magnitude lower than that inferred from convective rates or glacial rebound. While anisotropy is neglected for the purposes of computing the velocity field, the simulations that follow still compute the texturing based on the polycrystal model, including the single-crystal behaviour for olivine and the lower bound-linking hypothesis. In this respect, coupling between the macroscopic velocity field and the evolving microstructure is only from the velocity field to the microstructure, and not from the microstructure to the velocity field. This is discussed in more detail in the following sections.

§ 6. Results

The convection cell is 2900 km deep and 3000 km wide. Within this region are three zones: the lower mantle extends from 650 to 2900 km depth across the width of the cell; the upper mantle extends from the bottom of the crust to the lower mantle, and also across the full width of the cell; the crust extends from the surface to the top of the upper mantle, varying in thickness from 50 km (along the boundary with upwelling) to 125 km (along the boundary with subduction). The cell geometry is shown schematically in figure 2. Along the bottom of cell (lower extent of the lower mantle), no vertical velocity is allowed. Along both lateral surfaces, no horizontal velocity is allowed. The crust is assumed rigid and, at the boundary between the upper mantle and the crust, the velocity of the upper mantle is required to be tangential to the crust–upper mantle boundary. It is not necessary to model the crust explicitly with these boundary conditions, and so only the upper and lower

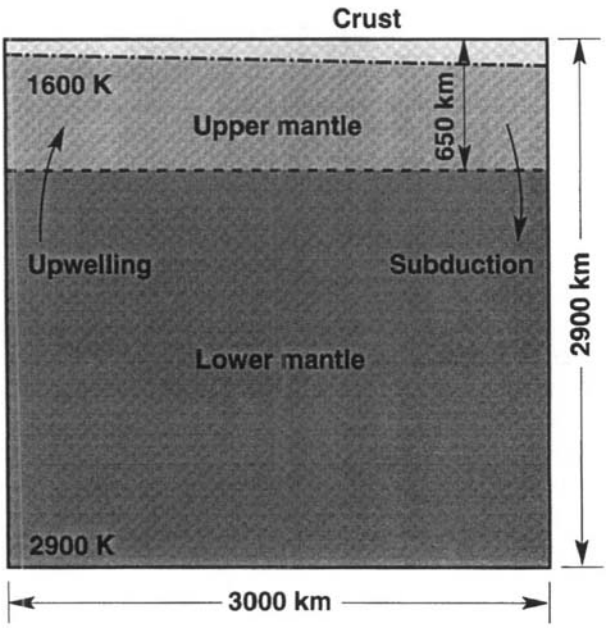

Figure 2. Schematic diagram of the convection cell showing the upper and lower regions of the mantle and the crust.

Table 2. Parameters used in the simulations (Turcotte and Schubert 1989, Blankenbach 1989). If ranges are given, the first value is for the top of the mantle and the second for the bottom of the mantle.

Quantity	Symbol	Units	Value
Density	ρ	$kg\,m^{-3}$	$4(3.4–5.6) \times 10^3$
Heat capacity	C_p	$J\,kg^{-1}\,K^{-1}$	1.25×10^3
Thermal conductivity	k	$W\,m^{-1}\,K^{-1}$	5
Volumetric thermal expansion	α	K^{-1}	2.5×10^{-5}
Gravity	g	$m\,s^{-2}$	$9.8(9.86–10.68) \times 10^{18}$
Young's modulus	E	Pa	$(1.6–7.6) \times 10^{11}$
Compressibility	β	Pa^{-1}	$7.5(8.0–1.5) \times 10^{-12}$
Kinematic viscosity	ν	$m^2\,s^{-1}$	$2.5 \times 10^{19-17}$
Dynamic viscosity $\mu = \nu\rho$	μ	Pa s	$1 \times 10^{21-23}$

mantle zones have been discretized with finite elements. The top surface of the mantle is required to be 1600 K; the bottom surface of the lower mantle is fixed at 2900 K. The lateral boundaries are adiabatic.

A total of 360 higher-order isoparametric elements are used to discretize the full mantle: 120 in the upper mantle and 240 in the lower mantle. A Eulerian procedure is employed, so the elements are spatially fixed and mantle material flows through them. Within each element resides an aggregate of 1000 crystals that describes the texture. Each aggregate is numerically interrogated to determine average properties for its element. The crystal orientations for every aggregate must be updated to account for the evolution of texture. This is accomplished by integrating the equations for the lattice reorientation rate along the streamline leading to the element centroid. The connection between the macroscopic scale of the convective flow and that of the individual crystals is made using the equilibrium-based linking hypothesis.

Bulk properties of the mantle were chosen in accordance with the geodynamics literature (Turcotte and Schubert 1989) and benchmark calculations (Blankenback 1989). Corresponding values are listed in table 2. Values used in the present simulations correspond to the centre of this range. Figures 3 and 4 illustrate the temperature distribution and the velocity field when convection has reached a steady state. Both conform closely with our previous calculations (Chastel *et al.* 1993) and with models of other investigators (for example Turcotte and Oxburgh (1967), Hager and O'Connell (1981) and King *et al.* (1990)) and display patterns dominated by convective heat exchange.

The texture patterns for the element centroids of the upper mantle are presented in figure 5 as [100] pole figures. As in our previous model (Chastel *et al.* 1993), great heterogeneity is observed, vertically and laterally, with regions having strong texture while others have almost random orientation distributions. The uppermost layer is strongly textured, but immediately underneath there is a fairly isotropic layer. The centre of the cell is again strongly textured. All pole figures display a statistical diadic symmetry, consistent with two-dimensional (plane-strain) deformation. The pole figures have no mirror planes because the deformation has a simple shear component. Figure 6(*a*) and (*b*) show enlargements of pole figures 1 and 7 of the second row (from the top), which will be referred to as points 1 and 7 in the following discussion.

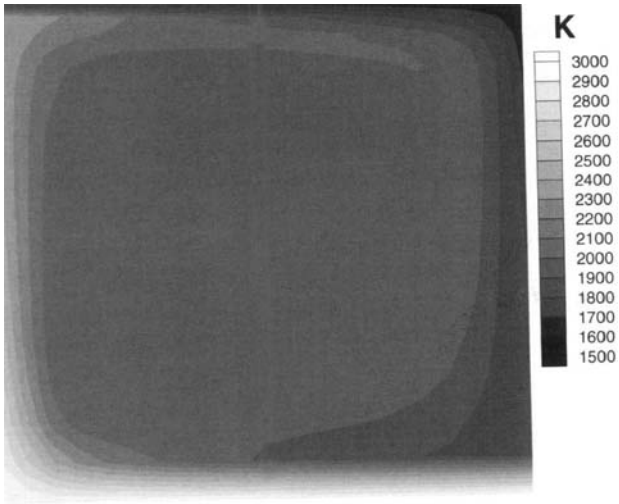

Figure 3. Temperature distribution during convection showing the effects of upwelling (on the left) and subduction (on the right).

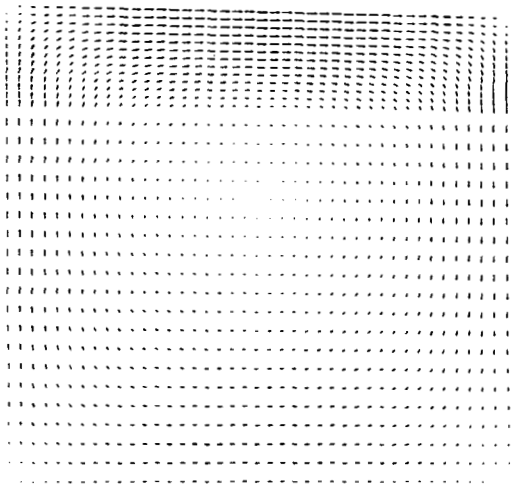

Figure 4. Convective velocity field shown using scaled vectors directed tangent to the flow.

In this case the discrete orientation distribution (OD) was entered into a continuous three-dimensional orientation space and smoothed with 7.5° and 30° filters (texture calculations and representations were done with BEARTEX (Wenk *et al.* 1998)). This OD was then used to calculate continuous [100] pole figures. Both locations display texture, point 1 is clearly textured more strongly than point 7. This can be quantified (table 3): the texture index F_2, a quantitative measure of the overall texture strength, is for the 7.5° smoothed orientation distributions five times higher for the first than the second location. It is also expressed in maximum pole densities in [100] pole figures. For figure 6(*a*), it is 26 MRD while, for figure 6(*b*), it is

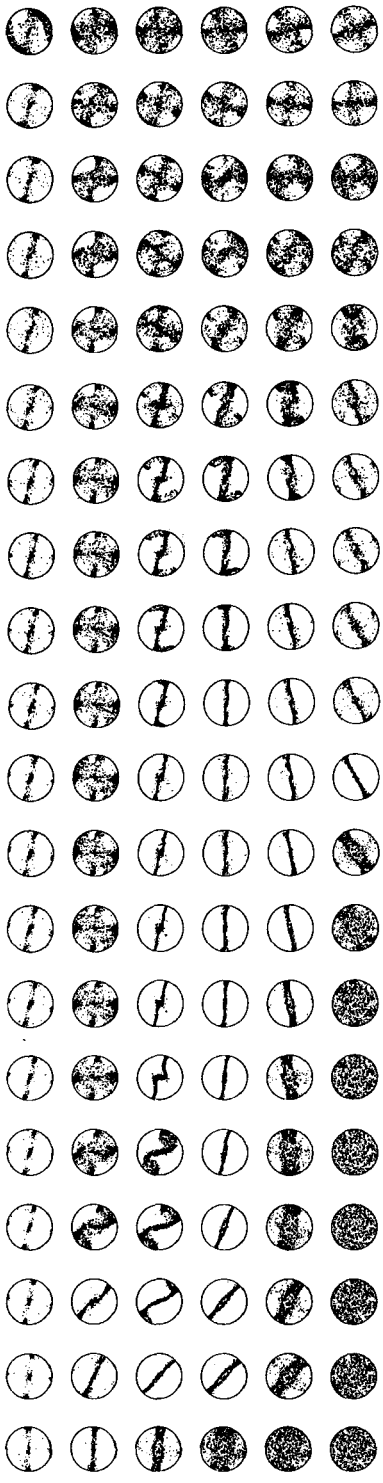

Figure 5. [100] pole figures displayed at the element centroids of the upper mantle (not to scale). Bottom is upwelling, left is horizontal spreading, top is subduction and right is lower mantle boundary.

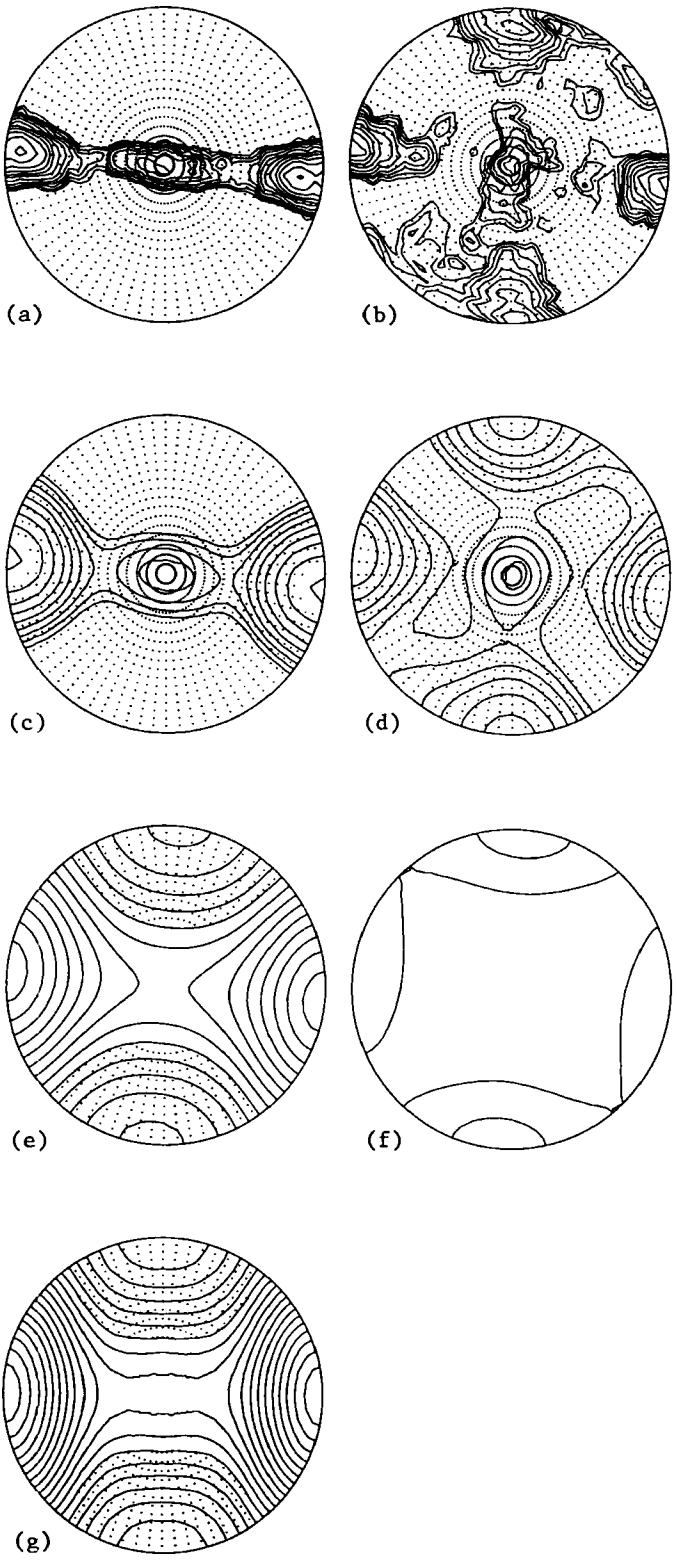

Table 3. Quantitative data on texture strength at points 1 and 7 of figure 6, and p-wave velocities, including single-crystal (X) values: MRD, multiples of random distribution.

Location	F_2	F_2 smoothed 7.5° at [30°]	OD (MRD) maximum 7.5°[30°]	[100] (MRD) maximum 7.5°[30°]	V_p (m s^{-1}) minimum 7.5°[30°]	V_p (m s^{-1}) maximum 7.5°[30°]
1	141	39 [6.9]	148 [20]	26 [8.5]	6776 [6820]	8061 [7914]
7	63	8 [1.7]	40 [4.9]	14 4.0]	7204 [7228]	7447 [7398]
X					6633	8485

14 MRD. These values both indicate a strongly textured condition. Part of this is due to the limited number of single orientations, even though we expanded from 200 crystals in every aggregate in the previous study to 1000 in the present work. As Matthies and Wagner (1996) have shown, the texture strength decreases with a $1/n$ relationship, where n is the number of orientations in the sample. The second reason is that most polycrystal plasticity models predict textures that are too strong. It can be attributed to the simplified assumption of pure slip, while in reality the evolution of the dislocation structure is much more heterogeneous within a crystal and, in the case of olivine, deformation by slip is accompanied by recovery. We shall show later that this overestimation of the texture strength has little effect on the elastic and seismic properties.

The evolution of texture is best evaluated by tracing material flow along various streamlines as shown in figure 7. In the lower mantle the material is assumed to be isotropic. When it enters the upper mantle and transforms to olivine, the texture evolution begins. Strong preferred orientation develops during upwelling with high shear. The pattern changes as the flow lines change direction from vertical to horizontal. During horizontal spreading, orientation changes are minimal. Finally, during subduction, a new pattern develops which is generally weaker but does not revert to randomness at the interface with the lower mantle. In our model the time for the convection path of an outer streamline in the upper mantle is about 120×10^6 years, corresponding to a spreading velocity of 2 cm year^{-1}.

If the orientation distribution and the tensor properties of the single crystal are known, then the physical properties of the textured polycrystal can be calculated by appropriate averaging. In the case of the mantle, elastic properties are of main interest. The single-crystal elastic stiffness values are given in table 4 for olivine. Using these values, averaging over all 1000 crystallites in each cell was performed with the self-consistent method assuming a spherical grain shape (Tomé 1998). From the averaged elastic constants and the density (4.5 g cm^{-3} for the central region of the

Figure 6. Preferred orientation patterns and seismic anisotropy for two selected points (point 1 during upwelling with strong texture (*a, c, e*) and point 7 during spreading with weaker texture (*b, d, f*); compare figures 5 and 8. (*a–d*) [100] pole figures were obtained by calculating a continuous OD and then smoothing the OD with (*a*), (*b*) 7.5° and (*c*), (*d*) 30° filters and recalculating from this smoothed OD the pole figures. Logarithmic contours are used (0.5, 0.7, 1.0, 1.4, 2.0 and 2.4. 4.0 MRD dot pattern below 1 MRD) with equal area projection. Longitudinal p-wave velocity propagation for (*e*) and (*f*) correspond to pole figures (*c*) and (*d*); (*g*) gives velocities for an olivine single crystal. Linear contours are shown with a contour interval of 100 m s^{-1} and the dot pattern below 7200 m s^{-1}. Compare table 3 for numerical data.

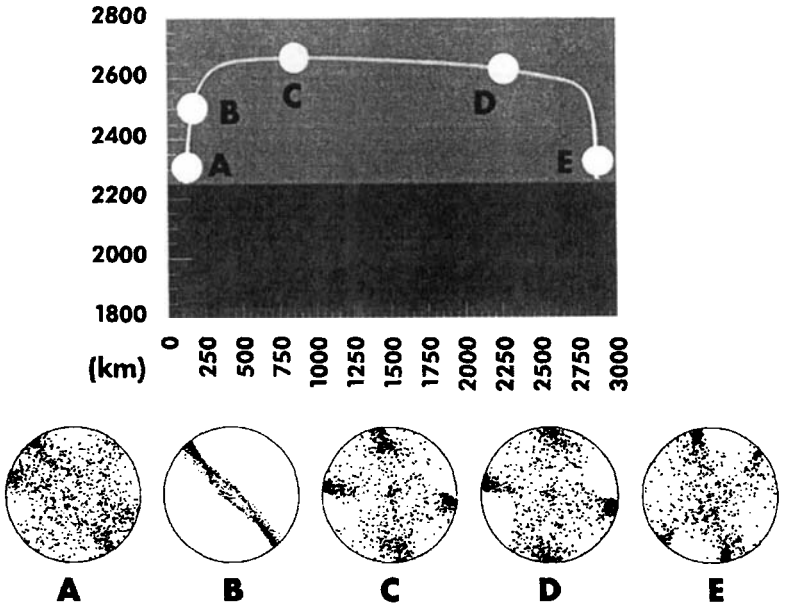

Figure 7. [100] pole figures along one streamline illustrating the evolution of texture for a rock traveling near the cell perimeter. Pole figures A–E correspond to positions A–E respectively.

Table 4. Single-crystal stiffness (Simmons and Wang 1971); Voigt notation.

C_{11} (GPa)	C_{12} (GPa)	C_{13} (GPa)	C_{22} (GPa)	C_{23} (GPa)	C_{33} (GPa)	C_{44} (GPa)	C_{55} (GPa)	C_{66} (GPa)
324	59	79	249	78	249	66.7	81	79.3

mantle), propagation surfaces for longitudinal (p) and transverse (s) waves were calculated, with those for p-waves shown for all element centroids in figure 8. The velocity maps are shown in equal area projection. We are aware that both the elastic constants and the density change with temperature and pressure, but in our representation we used constant values to emphasize the effects of anisotropy. All deviations from the value $7280\,\mathrm{m\,s^{-1}}$ for an isotropic polycrystal are due to texture. Similar to the pole figures in figure 5, there are large deviations from isotropy and also a heterogeneous distribution of anisotropy over the convection cell. Since the flow pattern is two dimensional, the deformation corresponds to plane strain, and textures and velocity surfaces have statistically a symmetry plane and a two fold rotation axis perpendicular to it. Overall, there is a correspondence between fast velocities and [100] concentrations, since [100] is the fast single-crystal direction. If earthquake travel times were recorded from waves which pass through the upper mantle at large angles, zones with high anisotropy would mainly appear as low velocity zones, since fast [100] directions are dominantly horizontal.

For two locations, designated by points 1 and 7, enlarged p-wave velocity patterns are shown in figure 6(*e*) and (*f*) and compared with the pattern for an olivine single crystal (figure 6(*g*)). The single-crystal pattern has two mirror planes, consistent with the orthorhombic symmetry of olivine. The highest velocity, along [100], is

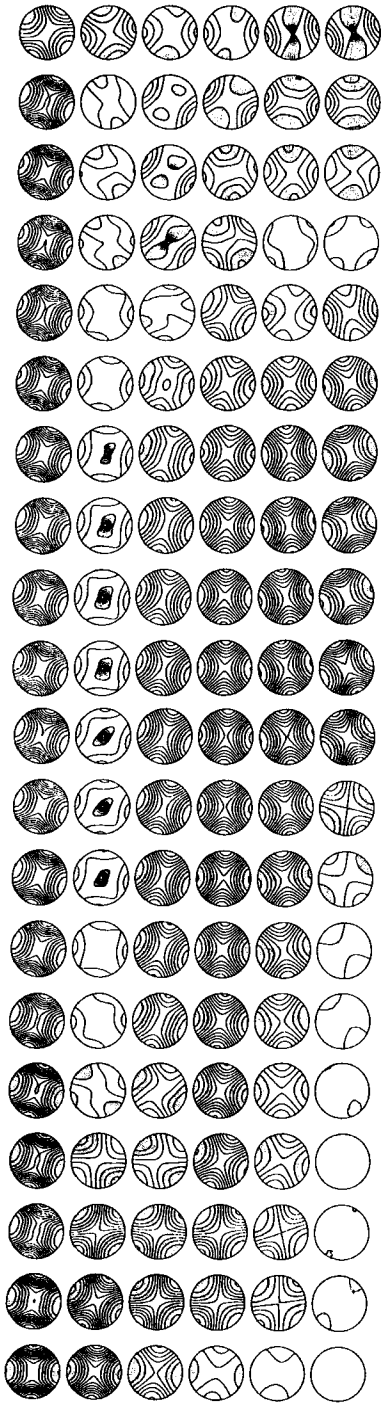

Figure 8. Longitudinal p-wave propagation surfaces at the elements centroids of the upper mantle corresponding to texture patterns shown in figure 5. Linear contours are shown with a contour interval of $100\,m\,s^{-1}$ and the dot pattern below $7200\,m\,s^{-1}$. (Bottom is upwelling, left is horizontal spreading, top is subduction and right is the lower mantle boundary.)

$8485\,m\,s^{-1}$ and the lowest is $6633\,m\,s^{-1}$. The polycrystalline patterns have a dyad, consistent with the texture symmetry. One pattern (point 1) shows a very strong anisotropy, close to that of a single crystal. In contrast, the second pattern (point 7) is almost isotropic. It needs to be emphasized that the anisotropy of a polycrystalline property depends not only on the texture strength but also on the particular texture pattern. In the case of point 7, two [100] maxima compete. Fourth-rank tensor properties, such as those of olivine, are very smooth surfaces, as is evident from figure 6 (*g*). This means that an average over a strongly textured sample is also quite smooth. Because of this, there is no need for an extremely strong texture to produce strong anisotropy. In other words, one does not need the exaggerated texture strength of the simulations to produce similar p-wave anisotropy patterns. Using a Gaussian filter of 30° width at half-maximum, we have smoothed the OD from which the [100] pole figures in figure 6 (*a*) and (*b*) were calculated, which greatly reduces the texture strengths at the two locations (figure 6 (*c*) and (*d*) and table 3) and brings both closer to observed fabric patterns (Nicolas *et al.* 1971). This much smoother texture has the same type and produces almost identical results for seismic velocities (table 3). In the model convection cell the highest velocity is $8100\,m\,s^{-1}$, while the lowest is $6800\,m\,s^{-1}$. The difference between the highest and lowest is about 60% of the single-crystal difference. Such seismic anisotropies are typical of rocks that presumably were deformed in the upper mantle.

In addition to the local averages, averages have been computed over larger scales (figure 9), particularly for regions of upwelling and spreading. The upwelling result is computed over a slab located at the upper left corner of the convection cell; the slab dimensions are 200 km depth and 300 km width. The spreading result is

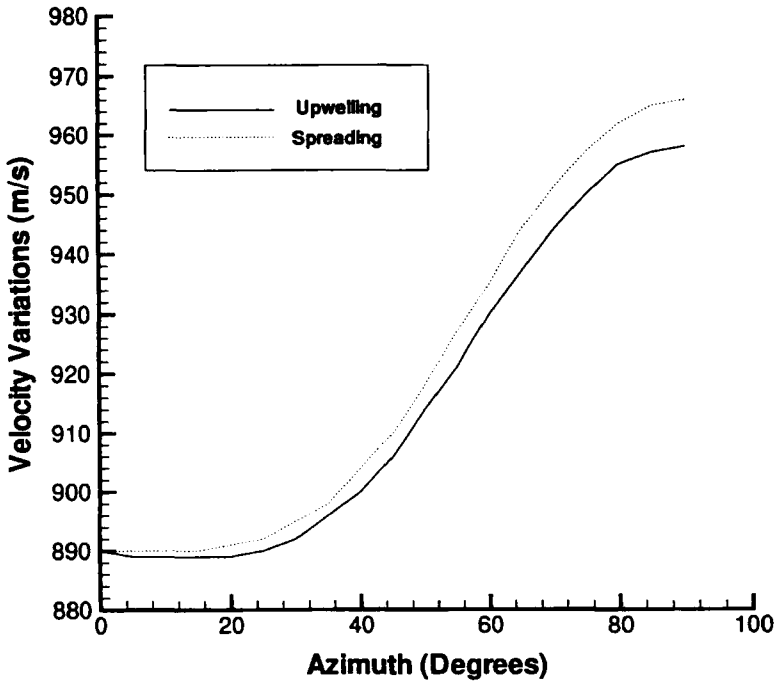

Figure 9. Seismic velocity variations in regions of upwelling and spreading.

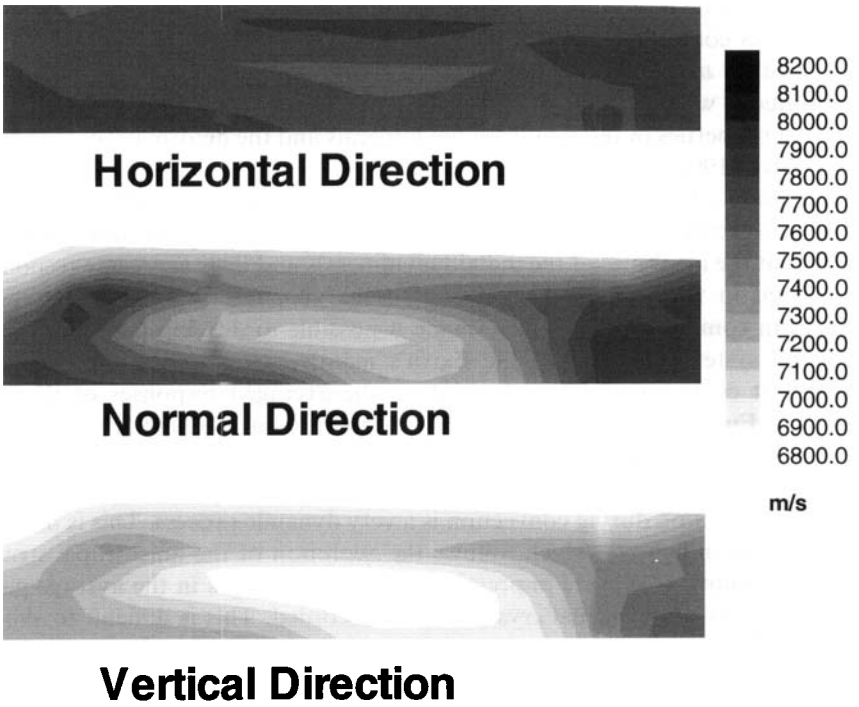

Figure 10. Seismic velocity distributions over the upper mantle corresponding to horizontal, vertical and normal (transverse) propagation directions.

computed over a slab that is adjacent to the crust boundary and is halfway between the upwelling and subducting boundaries; the slab dimensions are 100 km depth and 500 km width. The figures show the azimuthal variation in p-wave velocity, as would be observed with surface waves (horizontal). The velocity variation is 5–10%, in good correspondence to observed data from Hawaii (Morris *et al.* 1969), the Mendocino ridge (Raitt *et al.* 1969) and the southern Pacific (Nishimura and Forsyth 1989).

Finally contour maps of vertical, horizontal and normal velocities (again, assuming constant density and single-crystal properties) are presented for the full convective cell. This represents the local velocities if corresponding seismic waves were propagating in the corresponding directions (figure 10). Owing to the two-dimensional approach, deviations from average in the normal direction are minimal. However, in the other two maps there are again variations of 5–10% with patterns resembling seismic tomography maps (Anderson and Dziewonski 1984).

§ 7. Discussion

In a few places, mantle rocks have been transported to the surface and juxtaposed with the crust through irregularities of the convection process. These rocks commonly exhibit a strong preferred alignment of olivine crystals (Nicolas *et al.* 1971) and seismic anisotropy (Christensen 1984). Specifically, preferred orientation patterns of olivine in naturally deformed rocks are often slightly asymmetric to the flow plane (Mercier 1985, p. 428). On a larger scale, seismic waves, generated by

earthquakes, travel more rapidly perpendicular to ocean ridges than parallel to them over distances comparable with dimensions of continents (for example Morris *et al.* (1969), Raitt *et al.* (1969) and Nishimura and Forsyth (1989)). These observations are reproduced with our model. Anisotropy on such a large scale originates in the directional properties of the rock-forming minerals and the deformations that induce texture (Silver 1996).

Behaviours observed on scales associated with seismic observations can be derived consistently from properties observed in rocks. A test of such hypotheses requires that the attributes of the individual minerals and their aggregate response be incorporated in the mathematical model of the geophysical process in question. Advances in computing power have made it possible to develop numerical models of physical systems as large as the Earth's mantle, while basing the mechanical properties at every computational point on the averaged responses of thousands of crystals. Further, the changes in the properties that accompany deformation enter directly through the evolution of texture in the theory of plasticity for polycrystals.

Texture evolution during convection is a very dynamic process. This is illustrated to some extent in figure 7 which follows the evolution of the anisotropic structure along a streamline. It is more impressive if not only changes in the average pattern but the rotations of individual crystallites are recorded. This is difficult to show on paper. For this purpose we have prepared an educational video (Wenk *et al.* 1999) that illustrates the rapid changes, particularly during upwelling.

It must be emphasized that the details of the anisotropy distribution in our model mantle depend on many assumptions, such as material properties, dimensions of the convection cell, and boundary conditions. The convection cell of our model may not exist anywhere in the real Earth. However, the general anisotropy variations which we predict are not highly sensitive to any of the assumptions, and it is likely that they do occur. In particular, the heterogeneous distribution of regions with low and high anisotropy, changes in anisotropy over 500–1000 km, and magnitudes of anisotropy of 5–10% should be present in any convection cell composed of crystalline material which deforms by dislocation movements. The model establishes that velocity differences of 5–10% must be present in the upper mantle due to anisotropy. This is similar to differences inferred from phase transformations (Schubert *et al.* 1975, Tackley 1996), temperature differences and presence of partial melt (Sato *et al.* 1996).

Anisotropy in the upper layer of the upper mantle is well established and displays regular patterns related to plate motions (Tanimoto and Anderson 1885). These patterns have been interpreted by some as ancient rigid markers that can indicate the flow behaviour (Silver 1996). Others interpret it as a dynamic pattern that is recent and constantly created (Vinnik *et al.* 1989). The convection model is more supportive of the latter view. However, the fact that texture patterns barely change during spreading also fits the former interpretation that fast velocities in the upper mantle can be used to infer the flow direction. Note, however, that the empirical relationship connecting microscopic slip direction, fast wave propagation direction and macroscopic flow direction is only approximate and specific for olivine. In detail the fastest polycrystal direction is inclined to the flow direction, but to resolve such deviations is beyond the present precision of seismic observations. The relationship between slip direction and fast wave propagation is purely accidental and does not apply to all slip systems.

It has been quite surprising to see that the maps of velocity deviation from average (figure 10) have a resemblance to tomography maps, suggesting that perhaps part of the observed velocity deviations may be due to anisotropy, since the Earth is not homogeneously covered by earthquake sources and receiver stations, and therefore locations on tomographic maps may be directionally biased. This ought to be investigated by taking into account ray paths from earthquake source to station, rather than averaging data. In particular, it ought to be determined if the anisotropy is truly averaged out in tomographic solutions. The rapidly accumulating data from seismic networks will help to answer some of these questions about local anisotropy in the inner Earth. Of particular importance are observations with s waves (Silver 1996).

In the future there will be a need to quantify the methodology and to develop the means to apply it to more realistic systems. To accomplish this, one has to advance from two-dimensional to three-dimensional finite-element formulations. The computational burden grows as the product of the number of elements in the mesh and the number of crystals describing the properties within an element. For systems needing both many finite elements to resolve the flow and many crystals at each point to represent the properties, parallel computing capabilities are required (Beaudoin *et al.* 1993, Dawson and Marin 1997).

In our model we have assumed that deformation occurs solely by dislocation movements by slip. This is of course not the case. In addition, one has to expect recovery (dislocation climb) and recrystallization. Recovery is not a great concern since it does not produce texture and anisotropy. Recovery and diffusion in general may reduce the texture strength relative to pure slip. Dynamic recrystallization is pervasive and implications have been discussed by Karato *et al.* (1993). Experiments (AveLallemant and Carter 1970, Zhang and Karato 1995) and recent modelling of dynamic recrystallization (Wenk and Tomé 1999) suggested that recrystallization textures of olivine are similar to deformation textures but this needs to be further corroborated and included in the finite-element simulations. Based on analogy with other materials, detailed orientation patterns during deformation and dynamic recrystallization may be different, but overall strengths are similar and lead to similar anisotropy variations.

An important issue is the effective viscosity of the mantle. This topic has occupied geophysicists and materials scientists for many years and it is still not resolved (Stocker and Ashby 1973, Weertman and Weertman 1975, Weertman 1978, Nataf and Richter 1982, Sato 1991, Tackley 1996). The viscosity is largely inferred from indirect observations of glacial rebound (Peltier 1986, Forte and Peltier 1991). If, instead, one estimates the viscosity from experimentally determined data for slip of single crystals (Bai *et al.* 1991) (the critical resolved shear stresses and strain rate sensitivity), the effective viscosities for mantle convection are orders of magnitude too low. It is for this reason that an isotropic viscosity was employed in the finite-element simulations presented here, since a low viscosity implies a high Rayleigh number and very rapid convection. Introducing additional grain-boundary diffusion and recrystallization mechanisms would make the computed viscosities even lower. Obviously the relationships determined from single crystals are not compatible with the macroscopic description which is at present used. Possibly the temperature sensitivity of viscosity, extrapolated from the exponential law, is too high because at greater depths much stiffer garnet phases may occur in significant proportions in the upper mantle. There may be a (still undocumented)

influence of pressure on rate sensitivity, which perhaps could be established through molecular dynamic calculations. The simplified two-dimensional convective cell may further compound the viscosity issue as plane-strain motions often are an extreme case. Fully three-dimensional simulations would determine whether or not the simplified geometry is unduly sensitive to the low viscosity derived from experimental data.

The lower mantle is less problematic than the upper mantle since the assumption of superplastic flow can be applied (Ito and Sato 1991, Karato *et al.* 1995). For superplasticity no preferred orientation develops, if crystals are more or less equiaxed. Also, the viscosity, which in our case translates into the average anisotropic strain rate tensor of the polycrystal constitutive law, is for superplasticity related linearly to the stress.

Apart from the viscosity problem, other features need to be introduced into the anisotropic model. One is the issue of slab–mantle interactions (Ringwood 1990) and particularly slab penetration into the lower mantle (Creager and Jordan 1984). This requires a far more sophisticated treatment of phase changes than we are applying in the present model (Schubert *et al.* 1975, Bercovici *et al.* 1993, Nakakuki *et al.* 1994), not limited to the olivine–perovskite transformation but also considering garnet and spinel transformations in the upper mantle. The influence of partial melt during upwelling ought to be studied (Sato *et al.* 1996). All these will add to the velocity variations that are due to anisotropy. The goal of this study was to explore the effects of anisotropy alone.

§8. Conclusions

We have demonstrated that, for a compositionally and structurally homogeneous upper mantle, consisting of a single phase (olivine), preferred orientation of crystals that develops during convective flow introduces considerable heterogeneity. This heterogeneity is expressed as anisotropy of elastic constants and affects seismic wave propagation. This anisotropy may introduce p-wave velocity differences of 5–10%. It is important to recognize that the effect of intrinsic anisotropy due to crystal alignment on the propagation of seismic waves is of a similar magnitude as other features such as phase transformations, temperature gradients, existence of partial melt and compositional heterogeneities. We are well aware of these complications added by the real structure of the Earth, but the aim of this study was to isolate the anisotropy effect. It is clear that anisotropy ought to be included in any realistic geodynamic model and needs to be considered in seismic interpretations, as has long been advocated (Anderson and Dziewonski 1982). This can only be done with a model that takes into account the microscopic mechanisms that underlie deformation processes.

Acknowledgements

This work has been supported by the National Science Foundations through grant EAR 94-17580 and the Cornell Theory Center and by the Department of Energy through the Institute of Geophysics and Planetary Physics at Los Alamos National Laboratory. The authors wish to thank Chris Pelkie of Cornell Theory Center for assistance in the graphic presentation of the simulation results, Donald Boyce of Cornell University for assistance with the texture evolution computations, and Carlos Tomé of Los Alamos National Laboratory for assistance with the seismic velocity computations using the self-consistent approach.

References

ANDERSON, D. L., and DZIEWONSKI, A. M., 1982, *Geophys. J. R. Astr. Soc.*, **69**, 383; 1984, *Sci. Am.*, **251**, 60.

AVELALLEMANT, H., and CARTER, N. L., 1970, *Geol. Soc. Am. Bull.*, **81**, 2203.

BAI, Q., MACKWELL, S. J., and KOHLSTEDT, D. L., 1991, *J. geophys. Res.*, **96**, 2441.

BEAUDOIN, A. J., MATHUR, K. K., DAWSON, P. R., and JOHNSON, G. C., 1993, *Int. J. Plast.*, **9**, 833.

BEAUDOIN, A. J., MATHUR, K. K., DAWSON, P. R., KOCKS, U. F., and KORZEKWA, D. A., 1994, *Comput. Meth. appl. Mech. Engng.*, **117**, 49.

BERCOVICI, D., SCHUBERT, G., and TACKLEY, P. J., 1993, *Geophys. Res. Lett.*, **20**, 2599.

BLACKMAN, D. K., KENDALL, J. M., DAWSON, P. R., WENK, H. R., BOYCE, D., and MORGAN, J. P., 1996, *Geophys. J. Int.*, **127**, 415.

BLANKENBACH, B., 1989, *Geophys. J. Int.*, **98**, 23.

BUNGE, H. P., and BAUMGARDNER, J. R., 1995, *Comput. Phys.*, **9**, 207.

BUNGE, H. P., RICHARDS, M. A. , and BAUMGARDNER, J. R., 1996, *Nature*, **379**, 436.

CHASTEL, Y. B., DAWSON, P. R., WENK, H.-R., and BENNETT, K., 1993, J. geophys. Res., **98**, 17757.

CHRISTENSEN, N. I., 1984, *J. geophys. J. R. Astr. Soc.*, **76**, 89.

CREAGER, K. C., and JORDAN, T. H., 1984, *J. geophys. Res.*, **89**, 3031.

DAWSON, P. R., and MARIN, E. B., 1997, *Adv. appl. mech.*, **34**, 77.

DURHAM, W. B., and GOETZE, C., 1977, *J. geophys. Res.*, **82**, 5131.

ENGLEMAN, M. S., SANI, R. L., GRESHO, P. M., and BERCOVIER, M., 1982, *Int. J. Numer. Meth. Fluids*, **2**, 25.

FORTE, A. M. , and PELTIER, W. R., 1991, *J. geophys. Res.*, **96**, 20131.

GLATZMAIER, G. A., and SCHUBERT, G., 1993, *J. geophys. Res.*, **98**, 21969.

HAGER, B. H., and O'CONNELL, R. J., 1981, *J. geophys. Res.*, **86**, 4843.

HESS, H. H., 1964, *Nature*, **203**, 629.

ITO, E., and SATO, H., 1991, *Nature*, **351**, 140.

JOHNSON, C., 1987, *Numerical Solution of Partial Differential Equations by the Finite Element method* (Cambridge University Press).

KARATO, S.-Y., ZHANG, S., and WENK, H.-R., 1995, *Science*, **270**, 458.

KARATO, S., RUBIE, D. C., and YAN, H., 1993, *J. geophys. Res.*, **98**, 9761.

KING, S. D., RAEFSKY, A., and HAGER, B. H., 1990, *Phys. Earth Planet. Interion*, **59**, 195.

KOCKS, U. F., TOMÉ, C. N., and WENK, H.-R., 1998, *Texture and Anisotropy* (Cambridge University Press).

KOHLSTEDT, D. L., and GOETZE, C., 1974, *J. geophys. Res.*, **79**, 2045.

KUMAR, A., and DAWSON, P. R., 1996, *Comput. Meth. appl. Mech. Engng.*, **130**, 227; 1998, *ibid.*, **153**, 259.

MATHUR, K. K., DAWSON, P. R., and KOCKS, U. F., 1990, *Mech. Mater.*, **10**, 183.

MATTHIES, S., and WAGNER, F., 1996, *Phys. Stat. sol.* (b), **196**, K11.

MCKENZIE, D., 1979, *Geophys. J. R. Astr. Soc.*, **58**, 689.

MERCIER, J. C. C., 1985, *Preferred Orientation in Deformed Metals and Rocks: An Introduction to Modern Texture Analysis*, edited by H.-R. Wenk (Orlando, Florida: Academic Press), pp. 407–430.

MORRIS, G. B., RAITT, R. W., and SHOR, G. G., 1969, *J. geophys. Res.*, **74**, 4300.

NAKAKUKI, T., SATO, H., and FIJIMOTO, H., 1994, *Earth Planet. Sci. Lett.*, **121**, 369.

NATAF, H. C., and RICHTER, F. M., 1982, *Phys. Earth Planer. Lett.*, **29**, 320.

NICOLAS, A., BOUDIER, F., and BOULLIER, A.-M., 1973, *Am. J. Sci.*, **273**, 853.

NICOLAS, J. L., BOUCHEZ, F., and MERCIER, J. C., 1971, *Tectonophysics*, **12**, 55.

NISHIMURA, C., and FORSYTH, D., 1989, *Geophys. J.*, **96**, 203.

PELTIER, W. R., 1986, *J. geophys. Res.*, **91**, 9099.

PRANTIL, V. C., DAWSON, P. R., and CHASTEL, Y. B., 1995, *Modeling Simulation Mater. Sci. Engng.*, **3**, 215.

RAITT, R. W., SHOR, G. G., FRANCIS, T. J. G., and MORRIS, G. B., 1969, *J. geophys. Res.*, **74**, 3095.

RINGWOOD, A. E., 1990, *Chem. Geol.*, **82**, 187.

SACHS, G., 1929, *Z. Ver. Deutsches Ing.*, **72**, 734.

SATO, H., 1991, *Geophys. J. Int.*, **105**, 587.

SATO, H., MURO, K., HASEGAWA, A., and HASHIZUME, K., 1996, *Proc. Japan Acad.* B, **72**, 129.
SCHUBERT, G., YUEN, D. A., and TURCOTTE, D. L., 1975, *Geophys. J.R. Astr. Soc.*, **42**, 705.
SILVER, P. G., 1996, *A. Rev. Earth Planet Sci.*, **24**, 385.
SIMMONS, G., and WANG, H., 1971, *Single Crystal Elastic Constants and Calculated Aggregate Properties* (Cambridge, Massachusetts: MIT Press).
STOCKER, R. L., and ASHBY, M. F., 1973, *Rev. geophys. space Phys.*, **11**, 391.
TACKLEY, P. J., 1996, *J. geophys. Res.*, **101**, 3311.
TACKLEY, P. J., STEVENSON, D. J., GLATZMAIER, G. A., and SCHUBERT, G., 1993, *Nature*, **361**, 699.
TANIMOTO, T., and ANDERSON, D. L., 1985. *J. geophys. Res.*, **90**, 1842.
TAYLOR, G. I., 1938, *J. Inst. Metals*, **62**, 307.
TAYLOR, G. I., and ELAM, C. F., 1923, *Proc. R. Soc.*, **102**, 643.
TOME, C. N., 1998, *Texture and Anisotropy*, edited by U. F. Kocks, C. N. Tomé, and H.-R. Wenk (Cambridge University Press), chapter 7.
TURCOTTE, D. L., and OXBURGH, E. R., 1967, *J. Fluid Mech.*, **28**, 29.
TURCOTTE, D. L., and SCHUBERT, G., 1989, *Geodynamics Applications of Continuum Physics to Geological Problems* (New York: Wiley).
VINNIK, L. P., KIND, R., KOSAREV, G. L., and MAKEYEV, L. I., 1989, *Geophys. J. Int.*, **99**, 549.
WEERTMAN, J., 1978, *Phil. Trans. R. Soc.* A, **288**, 9.
WEERTMAN, J., and WEERTMAN, J. R., 1975, *A. Rev. Earth planet. Sci.*, **3**, 293.
WENK, H.-R. (editor), 1985, *Preferred Orientation in Deformed Metals and Rocks: An Introduction to Modern Texture Analysis* (Orlando, Florida: Academic Press).
WENK, H.-R., BENNETT, K., CANOVA, G., and MOLINARI, A., 1991, *J. geophys. Res.* B, **96**, 8337.
WENK, H. R., CANOVA, G. C., BRECHET, Y., and FLANDIN, L., 1997, Acta metall. mater., **45**, 3283.
WENK, H.-R., DAWSON, P. R., and CHASTEL, Y. B., PELKIE, C., 1999, *Convection in the Earth's Mantle: Predicting Seismic Anisotropy Using Crystallographic Texture*, Video (Washington, DC: American Geophysical Union).
WENK, H.-R., MATTHIES, S., DONOVAN, J., and CHATEIGNER, D., 1998, *J. appl. Crystallogr.*, **31**, 262.
WENK, H.-R., and TOMÉ, C. N., 1999, *J. Geophys. Res.* (in the press).
ZHANG, S., and KARATO, S., 1995, *Nature*, **375**, 774.
ZIENKIEWICZ, O. C., and TAYLOR, R., 1990, *The Finite Element Method* (London: Wiley-Interscience).